Magnetic Field-Enhanced Learning-Based Inertial Odometry for Indoor Pedestrian

Yan Wang, Jian Kuang, You Li, and Xiaoji Niu

***Abstract*—Pedestrian dead-reckoning (PDR) is a vital technique in pedestrian localization. Compared with traditional PDR, learning-based inertial odometry has the advantages of smaller position drift and is insensitive to pedestrian motion patterns. However, the heading drift of the trajectory is still the dominant error source for the position error drift in these methods. This study focuses on providing a pedestrian trajectory estimation method with low drift by properly fusing learned-based inertial odometry and magnetometer measurements under an indoor scenario containing significant magnetic field disturbance. The proposed method reduces the impact of magnetic field disturbance by adopting a long-term average magnetic vector, which is far more stable than using local magnetic vectors. Meanwhile, the proposed method can estimate the magnetometer bias online rather than depending on pre-calibrated magnetometer measurements. The test results show that the proposed method can obtain superior positioning performance using uncalibrated raw magnetometer data compared to other methods, even using calibrated magnetometer data. Simultaneously, this method achieves a balance between algorithm accuracy and efficiency.**

***Index Terms*—Pedestrian Dead Reckoning (PDR), Inertial Navigation, AI-Based Methods, location-based services (LBS) Magnetic Field**

I. Introduction

Pedestrian positioning plays a vital role in the Internet of Things (IoT), location-based services (LBS), and augmented reality (AR). The existing high-accuracy positioning techniques generally rely on LiDAR, cameras, and wireless sensors. LiDAR-based simultaneous localization and mapping (SLAM) [1] [2] which relies on professional equipment, can provide stable and reliable high-precision positioning. However, LiDAR is heavy and power-hungry and is not suitable for pedestrians. Camera-based SLAM includes visual odometry (VO) [3] and visual-inertial odometry (VIO) [4] [5]-based built-in cameras, and the inertial sensor of the smartphone is a low-cost and high-precision positioning solution with the potential to be widely used. Unfortunately, VIO does not work well in low-textured and dynamic illumination environments [6]. Wireless sensor-based methods (e.g., ultra-wideband [7] and 5G [8]) rely on pre-arranged signal base stations. This cost is extremely high, which is unrealistic for large-scale indoor environments.

This work was supported by National Natural Science Foundation of China (Grant No.42174024). (Corresponding author: Jian Kuang)

J. Kuang and Y. Wang are with the GNSS Research Center, Wuhan University, Wuhan, Hubei, CO 430072 PR China (e-mails: kuang@whu.edu.cn; wystephen@whu.edu.cn;)

X. Niu is with the GNSS Research Center, Wuhan University, Wuhan, Hubei, CO 430072 PR China. He is also with the Artificial Intelligence Institute of Wuhan University. (e-mail:xjniu@whu.edu.cn)

You Li is with the State KeyLaboratory of Surveying, Mapping and Remote Sensing, Wuhan University, Wuhan 430072, China (e-mail: liyou@whu.edu.cn;).

An Inertial Measurement Init (IMU) can be used to provide 3D motion estimation independent of the external environment. Moreover, almost all wearable smart terminals (e.g., phones, watches, glasses) are equipped with IMU. Therefore, from the perspective of the system cost and sensor properties, the IMU-based method is ideal for providing pedestrian positions in actual applications. This function is known as a strapdown Inertial Navigation System (INS) [9]. However, the strapdown INS, which uses a consumer-grade IMU, cannot individually maintain the position accuracy for more than several seconds. This is because the position accumulation error of strapdown INS is proportional to the square of time, and the errors (e.g., biases, scale factor, noise) of the consumer-grade IMU are large and unstable. Thus, pedestrian dead reckoning (PDR) is used as an alternative to provide usable position estimations for pedestrians. PDR uses prior knowledge of human motion patterns to mitigate accumulation errors in PDR. More specifically, the PDR based on IMU typically uses a pedestrian gait motion pattern. By identifying and classifying pedestrian steps, the estimated step length can be adopted to correct the estimated INS velocity [10] [11] [12].

However, the motion patterns of pedestrians during walking are difficult to detect in real applications. Therefore, learning-based PDR methods have been proposed. This type of method estimates the velocity or displacement using raw IMU measurements and shows impressive accuracy compared with traditional PDR in experiments [13] [14] [15]. Learning-based PDR can be categorized into two groups.

The first group of methods, including IONet [13], RoNIN [14] and IDOL [16], uses magnetometer measurements. IONet estimates the 2D displacement using IMU measurements represented in a global frame. The conversion of IMU measurements from the device frame to the global frame uses the rotation estimated by the Android API. RoNIN is implemented based on a similar strategy, but with training and evaluation on a larger dataset. Meanwhile, other deep learning architectures include a temporal convolutional network (TCN), a residual network (ResNet), and long short-term memory (LSTM), which have been tested in field experiments. Both methods show better performance than traditional PDR. Therefore, the neural network inputs of IONet and RoNIN rely on the absolute orientation estimated by the Android API, and the Android estimate orientation uses magnetometer measurements. Thus, position accuracy is easily degraded in areas with a highly perturbed magnetic field.

The second group of methods is independent of magnetometer measurements, that is, TLIO [15] and [17]. [17] uses IMU raw measurements directly to estimate trajectory. TLIO [15] uses a multi-state Kalman filter (MSCKF) to fuse the neural network and strapdown INS model. Unlike IONet and RoNIN, TLIO uses the orientation estimated in MSCKF to convert IMU measurements into local gravity-aligned coordinates. This mechanism indicates that TLIO is independent of magnetometer measurements and is not affected by magnetic perturbations. This also implies that the heading of TLIO drifts over time and affects its long-term positioning accuracy of TLIO. Although TLIO can provide accurate relative positioning results, the positioning error is still significantly affected by the heading drift [16].

In theory, a magnetometer can provide heading observations by measuring the earth's magnetic field. However, direct constraint heading using magnetometer measurements is difficult to perform in indoor scenarios because magnetometer measurements are not reliable [18] [19]. More specifically, building materials and electronic equipment highly perturb the indoor magnetic field. The quasi-static magnetic field (QSF) technique, which uses only magnetic constraints in the quasi-static field, can effectively use magnetometer measurements to estimate heading in highly perturbed environments [20] [21]. The QSF can inhibit the increase in the heading error, but the heading error is still slightly accumulated. This indicates that heading drift is still the primary error source of PDR in long-term trajectory estimation. Furthermore, these methods can only use calibrated magnetometer measurements, which are difficult to obtain in real-world applications.

IDOL aims to solve this issue by training a neural network to estimate orientation based on inertial and magnetometer measurements. IDOL shows the ability to capture magnetic field perturbations. Therefore, its positioning accuracy outperformed that of RoNIN and TLIO in the experiment. The estimated orientation of the IDOL can be utilized to improve the positioning accuracy of RoNIN. However, learning-based orientation estimators may degrade in novel environments, as mentioned in [16]. However, it is difficult to collect data from every environment. However, this method cannot be used for magnetometer measurements with significant bias.

This paper proposed a graph-optimization-based system that fuses learning-based inertial odometry (AI-IMU) and magnetometer measurements to provide a global consistent heading estimation in magnetic disturbances. This study makes the following two major contributions:

- We found that the long-term mean value of the geomagnetic field is significantly more stable than the local magnetic field. The proposed system reduces the influence of local magnetic field disturbance by using the long-term mean value rather than the instantaneous value. Benefitted from this, the proposed system shows a 50% improvement in positioning accuracy in indoor scenarios.
- To deal with the frequent change of the magnetometer bias, we simplified the model of the magnetometer bias and performed real-time estimation and compensation. This property makes the proposed system user-friendly for consumer-grade devices since the demand for calibration before usage is avoided.

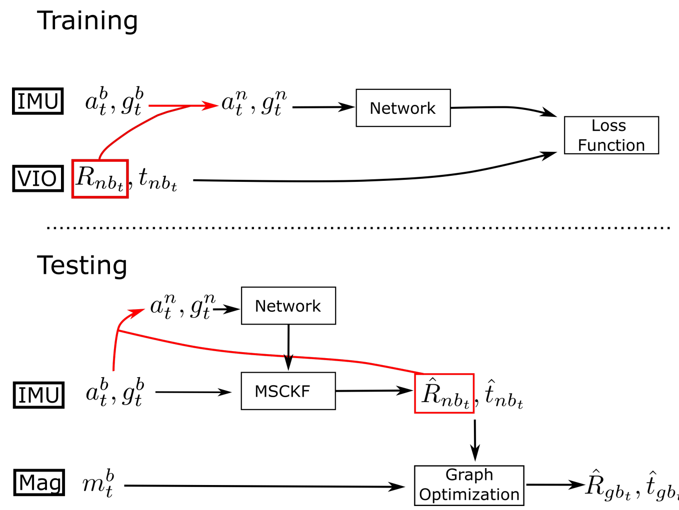

Fig. 1. Data flow of the proposed system.

The remainder of this paper is organized as follows: Section II briefly describes the entire system. Section III provides a detailed description of the solution. Section IV uses a field test to prove that the proposed method improves the accuracy. Section V summarizes this study.

II. System Overview

Compared with traditional PDR, learning-based inertial odometry indicates a gratifying positioning performance. However, the drift of the heading still causes the performance of the learning-based inertial odometer to drop significantly. The heading angle based on the magnetometer observation is an available information source that can effectively control the heading angle error. As mentioned in the introduction, using magnetometer observations to train the network model cannot guarantee that the positioning performance will not decrease in a new building environment. The phenomenon in which the main component of the environmental magnetic field vector is still a geomagnetic field is not limited to a single test environment. This makes the magnetic heading observation more universal. Therefore, this study combined network and traditional empirical models to form a robust pedestrian positioning solution.

As shown in Fig. 1, this system contains two stages named training and testing. The training stage uses visual-inertial odometry (VIO) to provide poses of IMU for training a network that can estimate 3D displacement based on IMU measurements represented in the navigation frame. This stage was introduced in a previous study by [22]. This study focused on using a magnetometer during the testing stage to improve position accuracy. The testing stage fuses the information from IMU, the pre-trained network, and magnetometer to provide a trajectory without heading drift and is not affected by local magnetic field disturbance. In this stage, the system comprises learning-based inertial odometry (denoted as AI-IMU) and a graph optimization estimator.

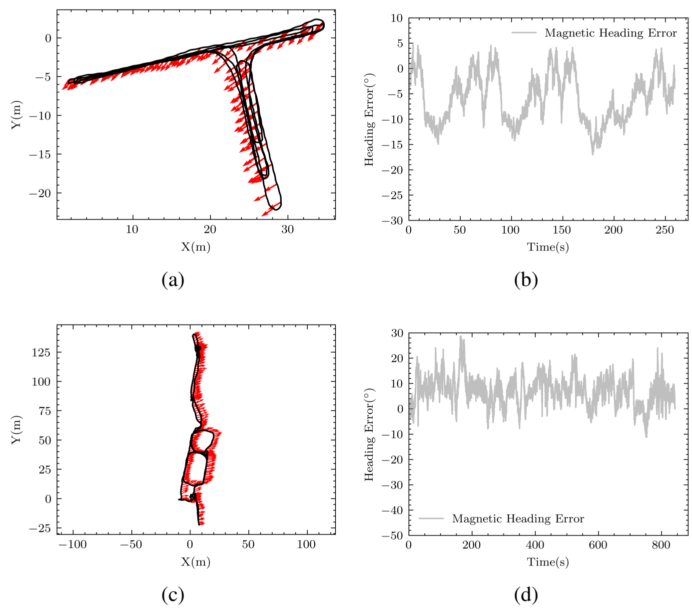

Fig. 2. Illustraction of magnetic field vector and magnetic field heading error. (a) and (c) gives magnetic field vector at each point of the trajectory A and B. (b) and (d) gives magnetic field heading error of the trajectory A and B.

The AI-IMU uses raw IMU measurements to provide 3D relative pose estimation, and consists of a neural network (denoted as Network in Fig. 1) and a Multi-State Cloning Kalman Filter (MSCKF). The neural network provides a 3D displacement between the beginning and the end of a sliding window, with the sliding window length being 1 s. The input of the neural network is IMU measurements in the sliding window, represented in a local gravity-aligned coordinate frame. To obtain a continuous and stable pose estimation, MSCKF is adopted to fuse the information from IMU mechanization and neural network (denoted as Network in Fig.1). INS mechanization is employed to predict the system state (including pose, velocity, and sensor biases) and the corresponding uncertainty, which uses IMU raw measurements.

The graph optimization estimator (denoted as the graph optimization in Fig. 1) uses relative 3D pose coming from AI-IMU and magnetometer measurements to estimate trajectory without drift of heading. Considering the computational cost, the estimator only estimates keyframes and utilizes a sliding window strategy. Specifically, the AI-IMU provides the relative pose and corresponding uncertainty between the current and previous keyframes, and the magnetometer provides magnetometer measurements of keyframes. The estimator builds absolute and relative orientation constraints based on magnetometer measurements to mitigate heading errors.

There are two main challenges in estimating a consistent global heading direction based on magnetic measurements in indoor environments. More specifically, these challenges include magnetic field perturbation and uncalibrated magnetometer biases.

For the first challenge, we realized that the long-term mean value of the geomagnetic field was not affected by the local magnetic field disturbances. Fig. 2 gives local magnetic field vectors and magnetic heading errors of two trajectories. Local magnetic field vectors are roughly in the same direction, but with significant perturbation at some point. The magnetic heading error represents the difference in the magnetic field vector direction from the first moment. The local magnetic field vector exhibits a significant disturbance, but the long-term magnetic field vector is stable and reliable. This is reasonable because building structures, obstacles, and other electronic devices can easily affect the local magnetic field around them; however, they cannot affect the magnetic field over a large area. To utilize this characteristic, we must save long-term magnetic field observations in the estimator and use this to obtain the long-term magnetic field average and constrain the heading. Thus, the estimator needs to store the magnetic field information for a sufficiently long time or keyframes.

For the second challenge, the observability of magnetometer biases originates from the change in pedestrian heading. To improve the observability and eliminate the influence of magnetic field perturbation, the estimation of magnetometer biases also relies on magnetometer observations stored for a sufficiently long time or keyframes. Simultaneously, multiple geomagnetic observations in a short period have information redundancy for the above two challenges because the magnetic field disturbance and the Earth's magnetic field cannot be distinguished in the short term. In summary, the designed algorithm requires long-term, low-frequency magnetometer observations to solve the two challenges we face. For example, we used a magnetometer observation for several hundred seconds at a frequency of 1 Hz to estimate heading. On the other hand, the AI-IMU relies on high-frequency information fusion to ensure the stability of track inference. Specifically, AI-IMU needs to save 10 keyframes every second to achieve a correction frequency of 10 Hz. However, the observation information of the AI-IMU is the displacement within a 1-second output by the neural network; therefore, its keyframe selection strategy is small in number but low in frequency.

Furthermore, it is unacceptable for real-time algorithms to implement high-frequency and long-term insertion of keyframes into one estimator. To bridge the difference between the two partial algorithms, this study proposes the aforementioned two-layer estimator. Specifically, the AI-IMU uses the output of MSCKF's high-frequency fusion neural network of the MSCKF to calculate pedestrian tracks. The graph optimization algorithm combines the AI-IMU output and low-frequency geomagnetic observations. Thus, the overall algorithm realizes full and effective use of various types of information and lower computing resource consumption.

III. Algorithm Description

A. Coordinate Definition

This study defines two groups of coordinate frames, as shown in Fig.3: coordinates adopted in the MSCKF and coordinates adopted in the graph-optimization estimator. These two groups of coordinate frames are adopted in two submodules (AI-IMU and graph optimization) individually. The only connection between these two groups is the relative pose between keyframes.

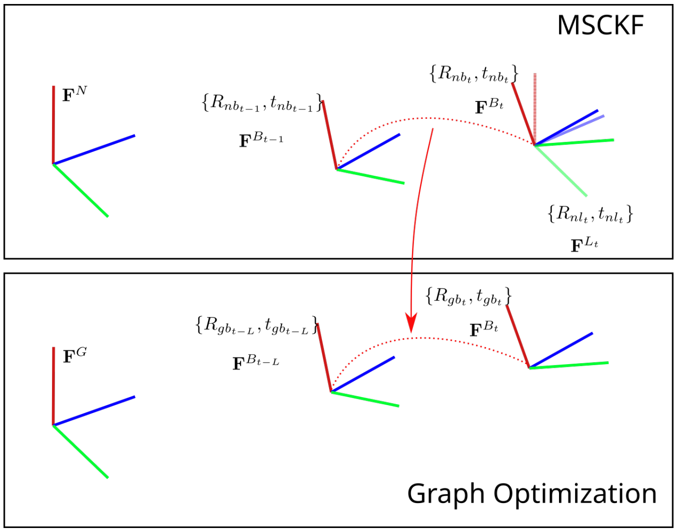

Fig. 3. Coordinate frames used in the proposed system. There are two groups of coordinate frames. The MSCKF uses $\mathbf{F}^N$, $\mathbf{F}^{B_t}$ and $\mathbf{F}^{L_t}$. The graph-optimization estimator uses $\mathbf{F}^G$, $\mathbf{F}^{B_t}$. Both $\mathbf{F}^N$ and $\mathbf{F}^G$ are gravity-aligned coordinate frames aligned with the center of IMU at the initial moment. The only connection between these two groups is relative poses between keyframes, marked as red dotted lines.

MSCKF uses three coordinate frames: the navigation frame is denoted as $\mathbf{F}^N$, the t-th body frame is denoted as $\mathbf{F}^{B_t}$, and the t-th local gravity-aligned coordinate is denoted as $\mathbf{F}^{L_t}$. The body frame aligns the coordinates of IMU at time t. $\mathbf{F}^N$ is the gravity-aligned coordinate system. It is aligned with the IMU center at the initial moment. $\mathbf{F}^{L_t}$ is the gravity-aligned coordinate frame. It has the same position and heading as that of $\mathbf{F}^{B_t}$. The MSCKF estimates 3D motion and IMU sensor bias. The 3D motion parameterized as the position ($\boldsymbol{t}_{nb_t}$) of the t-th body frame, rotation ($\boldsymbol{R}_{nb_t}$) from $\mathbf{F}^{B_t}$ to $\mathbf{F}^N$ and the velocity ($\boldsymbol{v}_{nb_t}$) of $\mathbf{F}^{B_t}$ in $\mathbf{F}^N$.

$\boldsymbol{R}_{nb_t}$ can be decomposed into three individual rotation matrices.

$$\boldsymbol{R}_{nb_t} = \boldsymbol{R}_{yaw_t}\boldsymbol{R}_{ptich_t}\boldsymbol{R}_{roll_t} \tag{1}$$

$\boldsymbol{R}_{yaw_t}$, $\boldsymbol{R}_{ptich_t}$, and $\boldsymbol{R}_{roll_t}$ denote yaw, pitch, and roll, respectively. According to the definition of $\mathbf{F}^N$ and $\mathbf{F}^{L_t}$, $\boldsymbol{R}_{yaw_t}$ represents the rotation from $\mathbf{F}^{L_t}$ to $\mathbf{F}^F$.

The graph-optimization estimator uses two coordinates: the global frame, denoted as $\mathbf{F}^G$, and the t-th body frame, denoted by $\mathbf{F}^{B_t}$. The global frame was the reference frame for the estimator. It is a gravity-aligned coordinate and is located at the position of IMU at the 0th moment. The magnetic reference field is represented by $\mathbf{F}^G$ and denoted as $\boldsymbol{B}^G$. The pose of two adjacent keyframes in the estimator is denoted as $\{\boldsymbol{R}_{gb_{t-L}}, \boldsymbol{t}_{gb_{t-L}}\}$ and $\{\boldsymbol{R}_{gb_t}, \boldsymbol{t}_{gb_t}\}$. The subscript L defines the time distance between keyframes. The implementation time was set at 1 s.

The raw IMU measurements at tth moment are denoted as $\boldsymbol{a}_t^{B_t}$ and $\boldsymbol{\omega}_t^{B_t}$. The magnetometer measurements represented in $\mathbf{F}^{B_t}$ at tth moment are denoted by $\boldsymbol{B}_t^{B_t}$. Furthermore, the IMU measurements represented in $\mathbf{F}^N$ are denoted by $\boldsymbol{a}_t^N$ and $\boldsymbol{\omega}_t^N$.

B. AI-IMU

1) System State Definition: The full system state at tth moment is defined as

$$\boldsymbol{X}_t = [\boldsymbol{s_t}, \boldsymbol{\eta_1}, ..., \boldsymbol{\eta_m}] \tag{2}$$

where $\boldsymbol{\eta}$ is the cloned system state, and $\boldsymbol{s}_t$ is the current system state. $\boldsymbol{s}_t$ and $\boldsymbol{\eta}$ are defined as follows.

$$\boldsymbol{s}_t = [\boldsymbol{t}_{nb_t}, \boldsymbol{v}_{nb_t}, \boldsymbol{R}_{nb_t}, \boldsymbol{b}_a, \boldsymbol{b}_g], \tag{3}$$

$$\boldsymbol{\eta}_i = [\boldsymbol{R}_{nb_i}, \boldsymbol{t}_{nb_i}] \tag{4}$$

$\boldsymbol{R}_{nb_t}$ denotes the rotation from $\mathbf{F}^{B_t}$ to $\mathbf{F}^N$. $\boldsymbol{t}_{nb_t}$ and $\boldsymbol{v}_{nb_t}$ denote the position and velocity of $\mathbf{F}^{B_t}$ in $\mathbf{F}^N$. $\boldsymbol{b}_a$ and $\boldsymbol{b}_g$ are the IMU accelemeter and gyroscopt bias, respectively. Hence, the dimension of the system is $15{+}6m$, where m is the number of cloned system states, and 15 is the dimension of s_t.

2) State Propagation: The filter propagates the system state using IMU raw measurements based on IMU mechanization. In pedestrian positioning, the walking speed of the pedestrian is low. Thus, the change in gravity orientation caused by IMU movement can be ignored. Gravity $\boldsymbol{g}^N$ is assumed equal during positioning. Furthermore, the Earth's spin is ignored. We assumed that the IMU only measured the rotation related to the navigation frame $\mathbf{F}^N$. The IMU mechanization utilized in this approach is defined asfollows:

$$\boldsymbol{R}_{nb_t} = \boldsymbol{R}_{nb_{t-1}} exp_{SO3}(\omega_t^{B_t}\Delta t) \tag{5}$$

$$\boldsymbol{v}_{nb_t} = \boldsymbol{v}_{nb_{t-1}} + \boldsymbol{g}^N + \boldsymbol{R}_{nb_t}(a_b^{B_t}\Delta t) \tag{6}$$

$$\boldsymbol{t}_{nb_t} = \boldsymbol{t}_{nb_{t-1}} + \frac{1}{2}(\boldsymbol{v}_{nb_t} + \boldsymbol{v}_{nb_{t-1}}) \tag{7}$$

where exp_{SO3} denotes the $SO(3)$-exponetial map.

3) Measurement Update: The measurement update of the AI-IMU uses the 3D relative displacement estimated by the neural network. The input of the neural network is IMU measurements represented in the local gravity-aligned coordinate frame $\mathbf{F}^{L_t}$. The network input is denoted by $\{\hat{\boldsymbol{a}}_{t-100:t}, \hat{\boldsymbol{\omega}}_{t-100:t}\}$. This implies that the latest 100 IMU measurements are represented by $\mathbf{F}^{L_t}$. Since the IMU samples 100Hz, the input is IMU measurements in the last 1 s. The neural network inference process is defined as

$$\{\hat{\boldsymbol{d}}_t^{L_t}, \Sigma_{\hat{\boldsymbol{d}}_t^{L_t}}\} = \textbf{Network}(\{\hat{\boldsymbol{a}}_{t-100:t}, \hat{\boldsymbol{\omega}}_{t-100:t}\}) \tag{8}$$

where $\hat{\boldsymbol{d}}_t^{L_t} \in \mathbb{R}^3$ and $\Sigma_{\hat{\boldsymbol{d}}_t^{L_t}} \in \mathbb{R}^{3\times3}$ are the displacement and the corresponding covariance matrix, respectively.

As described in Section III-A, the measurement function is defined as

$$h(\boldsymbol{X}_t) = \hat{\boldsymbol{R}}_{yaw_t}^T(\hat{\boldsymbol{t}}_{nb_{t-100}} - \hat{\boldsymbol{t}}_{nb_t}) = \hat{\boldsymbol{d}}_t^{L_t} + \boldsymbol{n}_{\hat{\boldsymbol{d}}_t^{L_t}} \tag{9}$$

$\boldsymbol{n}_{\hat{\boldsymbol{d}}_t^{L_t}}$ follows a normal distribution, $\mathcal{N}(0, \Sigma_{\hat{\boldsymbol{d}}_t^{L_t}})$. Furthermore, we employed a χ^2-test to avoid abnormal results provided by the network block.

4) Relative Pose and Uncertainty: In the proposed system, the AI-IMU functions as an odometer that outputs relative poses for further fusion. Specifically, we must provide the relative pose between $\{\hat{\boldsymbol{R}}_{nb_{t-L}}, \hat{\boldsymbol{t}}_{nb_{t-L}}\}$ and $\{\hat{\boldsymbol{R}}_{nb_t}, \hat{\boldsymbol{t}}_{nb_t}\}$. Covariance matrix for the relative pose is also necessary. The relative pose is defined as:

$$\Delta\hat{\boldsymbol{R}}_{b_t b_{t-L}} = \hat{\boldsymbol{R}}_{nb_t}^T \hat{\boldsymbol{R}}_{nb_{t-L}} \tag{10}$$

$$\Delta\hat{\boldsymbol{t}}_{b_t b_{t-L}} = \hat{\boldsymbol{R}}_{nb_t}^T (\hat{\boldsymbol{t}}_{nb_{t-L}} - \hat{\boldsymbol{t}}_{nb_t}) \tag{11}$$

$\Delta\hat{\boldsymbol{R}}_{b_t b_{t-L}}$ represents the rotation from $\mathbf{F}^{B_{t-L}}$ to $\mathbf{F}^{B_t}$, $\Delta\hat{\boldsymbol{t}}_{b_t b_{t-L}}$ denotes the position of $\mathbf{F}^{B_{t-L}}$ in $\mathbf{F}^{B_t}$. To model the uncertainty of this relative pose, we calculated the corresponding covariance based on the following equation:

$$\Sigma_{\{\Delta R_{\boldsymbol{b_t b_{t-L}}}, \Delta t_{\boldsymbol{b_t b_{t-L}}}\}} = \boldsymbol{H}_{rel} \boldsymbol{P}_t \boldsymbol{H}_{rel}^T \tag{12}$$

$\boldsymbol{H}_{rel}$ represents the Jacobian matrices of (10) and (11), respectively.

C. Graph-Optimization-Based Heading Fusion

1) Problem Definition: The graph optimization estimator fuses the relative pose and magnetometer measurements to provide a lower position drift rate. The factor graph is shown in Fig.4. The three states are estimated in the factor graph, including the keyframe pose $\{\hat{\boldsymbol{R}}_{gb_t}, \hat{\boldsymbol{t}}_{gb_t}\}$, magnetometer bias $\boldsymbol{b}_B$, and magnetic field vector $\boldsymbol{B}^G$. The estimator can be used for uncalibrated magnetometers by estimating the magnetometer biases online. Furthermore, we estimated the average magnetic field vector at the initialization stage and found that th average magnetic field did not change over the entire experimental area. The initialization stage is described in Section III-C2. Otherwise, we only keep the system state for a short period in the estimator. In detail, we maintain the 300 latest states in the estimator and select one keyframe per second. Therefore, the estimator contained the state in the last 300 seconds to estimate the average heading.

As mentioned before, we realize that the average magnetic field vector of a large area is not affected by magnetic field perturbation. More specifically, the heading estimated by the graph optimization was based on the average magnetic field vector of the last 300 s. Thus, this heading should be close to the actual heading and unaffected by the local magnetic field perturbation. Furthermore, to eliminate the oldest keyframe without loss of information, we adopted the marginalization technique, which has been widely employed in the sliding window graph-optimization problem. Section III-C3 provides the details of the marginalization technique.

The full state vector at moment t in the sliding window is defined asfollows:

$$\boldsymbol{X}_t = [\boldsymbol{R}_{gb_{t-nL}}, \boldsymbol{t}_{bg_{t-nL}}, \cdots, \boldsymbol{R}_{gb_t}, \boldsymbol{t}_{gb_t}, \boldsymbol{b}_B, \boldsymbol{B}^G] \tag{13}$$

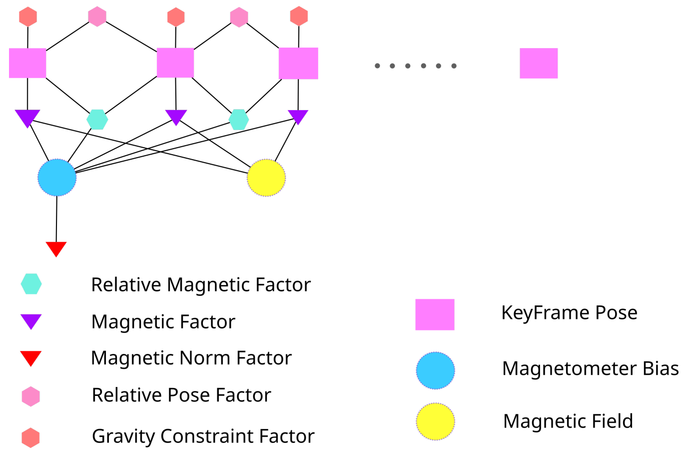

Fig. 4. An illustration of the factor graph for fusing AI-IMU and magnetometer. AI-IMU provides the relative magnetic factor and gravity constraint factor. The magnetic factor and relative magnetic factor are established based on magnetometer measurements. The magnetic norm factor constraints the norm of the local magnetic vector.

The maximum posterior estimation of the sliding window is as a result of the estimator. Specifically, $\boldsymbol{X}_t$ by minimizing the following cost function:

$$\begin{aligned} \boldsymbol{X}_t = & \\ \arg\min_{\boldsymbol{X}_t}\{ & \quad \|\boldsymbol{r}_{prior}\|^2 + \quad \|\boldsymbol{r}_{\|\boldsymbol{B^G}\|}\|^2_{\Sigma_{\|\boldsymbol{B^G}\|}} \\ & \sum \rho(\|\boldsymbol{r}_{odo}\|^2_{\Sigma_{odo}}) + \sum \rho(\|\boldsymbol{r_g}\|^2_{\Sigma_{\boldsymbol{g}}}) \\ & \sum \rho(\|\boldsymbol{r_B}\|^2_{\Sigma_{\boldsymbol{B}}}) + \sum \rho(\|\boldsymbol{r_{\Delta B}}\|^2_{\Sigma_{\Delta \boldsymbol{B}}}) \quad \} \end{aligned} \tag{14}$$

$\|\cdot\|^2_{\Sigma}$ represents the Mahalanobia norm of the residuals. $\boldsymbol{\rho}(\cdot)$ is the Huber norm [23] defined as

$$\boldsymbol{\rho}(s) = \begin{cases} 1 & s \geq 1 \\ 2\sqrt{s} - 1 & s < 1 \end{cases} \tag{15}$$

The cost function (14) defines a nonlinear least-squares problem. We used the Levenberg-Marquardt algorithm [24] [25] in Ceres Solver [26] to solve this problem. More specifically, we linearize (14) and solve the linearized equation iteratively. $\boldsymbol{r}_{prior}$ denotes prior constraint. $\boldsymbol{r_{B^G}}$ represents the strength constraint of $\boldsymbol{B}^G$. Generally, the main change in pedestrian movement is the heading, while the pitch and roll changes are minor. However, the observability of the magnetometer biases in the vertical direction is weak, and the biases can easily obtain an abnormal value. To mitigate this issue, it is necessary to constrain the strength of the total magnetic field vector to ensure that it is considered most of the time. $\boldsymbol{r_g}$ and $\boldsymbol{r}_{odo}$ represent the gravity orientation constraint and relative pose constraint, respectively, which are provided by the AI-IMU. $\boldsymbol{r_B}$ and $\boldsymbol{r_{\Delta B}}$represent the long -and short-term magnetic field constraints, which are based on magnetometer measurements. The details of the definition of the residual function are provided below.

$\boldsymbol{r}_{prior}$ represents the prior constraint and is defined as

$$\boldsymbol{r}_{prior}(\boldsymbol{x}) = \boldsymbol{A}(\boldsymbol{x} - \boldsymbol{b}) \tag{16}$$

$\boldsymbol{A}$ and $\boldsymbol{b}$ are defined based on prior distributions. Specifically, $\boldsymbol{x}$ can be recognized as following a normal distribution $\mathcal{N}(\boldsymbol{b}, (\boldsymbol{A}^T\boldsymbol{A})^{-1})$.

$\boldsymbol{r}_{\|\boldsymbol{B}^G\|}$ represents the total strength constraint on the magnetic-field vector. It is defined as

$$\boldsymbol{r}_{\|\boldsymbol{B}^G\|} = \|\boldsymbol{B}^G\| - \boldsymbol{Z}_{\boldsymbol{B}^G} \tag{17}$$

$\boldsymbol{Z}_{\boldsymbol{B}^G}$ represents the norm of the local average magnetic-field vector. Particularly, this value can be manually selected based on the theoretical model or average magnetic field vector estimated previously.

The residual of the relative pose $\boldsymbol{r}_{odo}$ is defined as

$$\begin{aligned} &\boldsymbol{r}_{odo}(\{\boldsymbol{R}_{gb_{t-L}}, \boldsymbol{t}_{gb_{t-L}}\}, \{\boldsymbol{R}_{gb_t}, \boldsymbol{t}_{gb_t}\}) = \\ &\begin{bmatrix} (\boldsymbol{R}_{gb_t}^T(\boldsymbol{t}_{gb_{t-L}} - \boldsymbol{t}_{gb_t})) - \Delta\boldsymbol{t}_{b_tb_{t-L}} \\ Log_{SO(3)}(\Delta\boldsymbol{R}_{b_tb_{t-L}}^T(\boldsymbol{R}_{gb_t}^T\boldsymbol{R}_{gb_{t-L}})) \end{bmatrix} \end{aligned} \tag{18}$$

where $\boldsymbol{t}_{b_tb_{t-L}}$ and $\boldsymbol{R}_{b_tb_{t-L}}$ are relative position and rotation represented in $\mathbf{F}^{B_{t-L}}$ and calculated based on (11) and (10). $Log_{SO(3)}(\cdot)$ represents the logarithm function for $SO(3)$ and outputs a three-dimensional vector. Furthermore, the covariance matrix Σ_{odo} is equal to $\Sigma_{\{\Delta R_{\boldsymbol{b}_t\boldsymbol{b}_{t-L}}, \Delta t_{\boldsymbol{b}_t\boldsymbol{b}_{t-L}}\}}$ which is calculated using (12). It is noteworthy that all linearization operations for rotation use the same formula. Specifically, we used perturbation on the right side of the rotation matrix.

The constraint of gravity orientation $\boldsymbol{r}_{\boldsymbol{g}}$ is defined as

$$\boldsymbol{r}_{\boldsymbol{g}}(\boldsymbol{R}_{gb_t}) = \boldsymbol{R}_{gb_t}\boldsymbol{g}^{B_t} - \boldsymbol{g}^G \tag{19}$$

$\boldsymbol{g}^{B_t}$ and $\boldsymbol{g}^G$ represent gravity vectors in $\mathbf{F}^{B_t}$ and $\mathbf{F}^G$ respectively. $\boldsymbol{g}^G$ is predefined, because the global frame is a gravity-aligned coordinate frame. $\boldsymbol{g}^{B_t}$ was calculated based on the rotation estimated by the AI-IMU. More specifically, it is calculated based on

$$\boldsymbol{g}^{B_t} = \boldsymbol{R}_{nb_t}^T\boldsymbol{g}^N \tag{20}$$

Because the relative pose residual $\boldsymbol{r}_{odo}$ uses relative rotation and displacement to constrain relative poses, the pitch and rolling angle related to the navigation frame implicated in the MSCKF of the AI-IMU will drift. Thus, we used the orientation of the gravity vector to constrain the absolute rolling and pitch angles.

The target devices discussed in this study are low-cost consumer-grade devices with limited quality and accuracy. We can ignore the scale factors and non-orthogonality corrections under this condition, which do not significantly affect magnetometer measurements. Indeed, magnetometer measurements are assumed to be affected only by biases and zero-mean Gaussian noise. The environmental magnetic field can be a combination of the geomagnetic field and magnetic field disturbance caused by buildings. Thus, the relationship between magnetometer measurements and the earth's magnetic field vector can be defined as

$$\boldsymbol{B}^B = \boldsymbol{R}_{gb}(\boldsymbol{B}^{\boldsymbol{G}} + \boldsymbol{B}^{\boldsymbol{E}}) + \boldsymbol{b}_B + \boldsymbol{n}_B \tag{21}$$

$\boldsymbol{B}^{\boldsymbol{B}}$ represents the magnetometer measurements. $\boldsymbol{B}^{\boldsymbol{E}}$ represents the magnetic field disturbance that varies spatially. It was impossible to estimate the absolute position without additional observations. In the proposed method, we mitigate the effect of this element by adopting an average magnetic field over a long term. $\boldsymbol{b}_B$ represents magnetometer bias. This can be estimated by rotating the magnetometer. For example, when the magnetometer rotates along the x-axis, the biases of the y-and z-axises can be estimated. $\boldsymbol{n}_B$ represents the random noise variables of the magnetometer, following a zero-center Gaussian distribution. According to this definition, we define the heading constraints as follows:

The heading constraint based on the magnetometer measurements $\boldsymbol{r}_{\boldsymbol{B}}$ is defined as

$$\boldsymbol{r}_{\boldsymbol{B}}(\boldsymbol{R}_{gb_t}, \boldsymbol{b}_B, \boldsymbol{B}^G) = \boldsymbol{R}_{gb_t}(\boldsymbol{B}^{B_t} - \boldsymbol{b}_B) - \boldsymbol{B}^G \tag{22}$$

$\boldsymbol{B}^{B_t}$ represents the magnetometer measurements at moment t. This residual $\boldsymbol{r}_{\boldsymbol{B}}$ provides a heading constraint. Otherwise, the Huber norm is applied to $\boldsymbol{r}_{\boldsymbol{B}}$ to avoid the effect of abnormal magnetometer measurements. Abnormal magnetometer measurements can be caused by abnormal local magnetic fields or other sources of error.

The relative heading constraint based on the magnetometer mesurements $\boldsymbol{r}_{\boldsymbol{\Delta B}}$ is defined as

$$\begin{aligned} &\boldsymbol{r}_{\boldsymbol{\Delta B}}(\boldsymbol{R}_{gb_{t-L}}, \boldsymbol{R}_{gb_t}, \boldsymbol{b}_B) = \\ &\qquad \boldsymbol{R}_{gb_{t-L}}(\boldsymbol{B}^{B_{t-L}} - \quad \boldsymbol{b}_B) - \boldsymbol{R}_{gb_t}(\boldsymbol{B}^{B_t} - \boldsymbol{b}_B) \end{aligned} \tag{23}$$

$\boldsymbol{r}_[\boldsymbol{\Delta B}]$ provides the relative rotation constraint based on magnetometer measurements for adjacent keyframes. To avoid the perturbation of the magnetic field, we applied the Huber norm to this residual. By combining $\boldsymbol{r}_{\boldsymbol{\Delta B}}$, $\boldsymbol{r}_{\boldsymbol{B}}$, and $\boldsymbol{r}_{\|\boldsymbol{B}^G\|}$, we can estimate $\boldsymbol{b}_B$ and $\boldsymbol{B}^G$ simultaneously. Specifically, $\boldsymbol{b}_B$ and $\boldsymbol{B}^G$ are observable when the IMU is rotated around any axis.

In summary, the proposed method models the heading, magnetic biases, and local magnetic field vector simultaneously rather than assuming that the magnetic biases are known through a calibration magnetometer before use. Thus, we can directly adopt measurements from uncalibrated magnetometers, which are convenient and user-friendly for consumer-level devices.

2) Initialization: We aim to design a method that can maintain the heading related to the first short period. As we recongnized that the average magnetic field vector in the long period can reflect the heading, the average magnetic field vector in the first sliding window is equal to that in any other sliding window. Therefore, we can estimate the average magnetic field vector for the first sliding window and use this average magnetic field vector to provide the heading constraint for the rest of the trajectory. It is noteworthy that the proposed method can estimate the trajectory during the initialization stage. The trajectory accuracy explained in the experiments does not ignore the initialization stage trajectories.

In the initialization stage, all the system states in $\boldsymbol{X}_t$ are estimated. The absolute position and heading are still unobservable in the system. To solve this problem, we fixed the pose of the first keyframe ($\{\boldsymbol{R}_{gb_0}, \boldsymbol{t}_{gb_0}\}$) and set a prior constraint on this pose. Furthermore, we first optimize (14) when there are more than ten keyframes contained in the sliding window. This strategy is helpful for avoiding the estimation of an abnormal magnetometer bias $\boldsymbol{b}_B$ and magnetic field vector $\boldsymbol{B}^G$ for the first time.

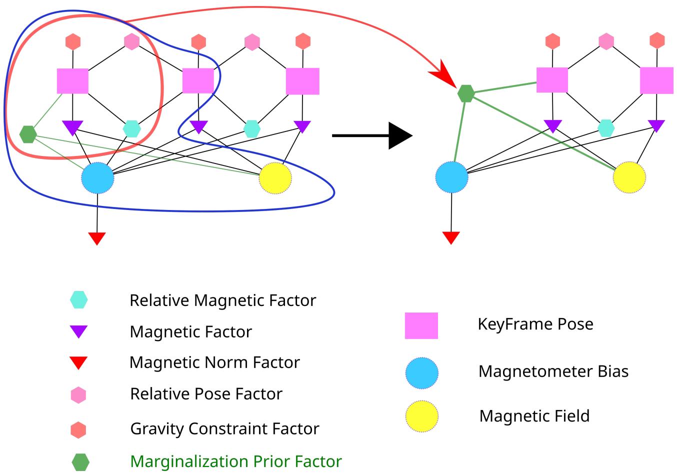

Fig. 5. Illustration of marginalization operation. The red circle selects the system state ready to be removed and relative residual factors. The blue line selects the sub-problem to be linearized. The green hexagon represents the prior factor.

When the sliding window grew to a particular length, we fixed the magnetic field vector $\boldsymbol{B}^G$. In this implementation, we fixed $\boldsymbol{B}^G$ when the sliding window contained 300 keyframes. In theory, by adopting the marginalization technique, we can obtain an optimal posterior estimation of the magnetic field vector, $\boldsymbol{B}^G$. Nevertheless, the marginalization operation uses a Gaussian distribution to approximate the marginalized residuals. This strategy causes loss of information. In this problem, the loss of information causes the magnetic field vector $\boldsymbol{B}^G$ to change slowly during the entire positioning process. Thus, we cannot maintain an absolute consistent heading if we do not fix the magnetic-field vector $\boldsymbol{B}^G$.

3) Marginalization: To eliminate computational cost, we employ a sliding window estimator. We adopted the marginalization technique [4] [27] to approximate the information contained in the removed residuals. It is widely used in visual odometry. When we aim to marginalize a set of states $\delta\boldsymbol{X}_m$, we must adopt the Schur-Complement operation for the sub-problem contained by $\boldsymbol{X}_m$ and relative system state $\boldsymbol{X}_r$. In detail, we linearize the subproblem at a particular linearization point to the linear system, defined as

$$\begin{bmatrix} \boldsymbol{H}_{mm} & \boldsymbol{H}_{mr} \\ \boldsymbol{H}_{rm} & \boldsymbol{H}_{rr} \end{bmatrix} \begin{bmatrix} \delta\boldsymbol{X}_m \\ \delta\boldsymbol{X}_r \end{bmatrix} = \begin{bmatrix} \boldsymbol{b}_m \\ \boldsymbol{b}_r \end{bmatrix} \tag{24}$$

$$\delta\boldsymbol{X}_m = \boldsymbol{X}_m - \boldsymbol{X}_m^{op} \tag{25}$$

$$\delta\boldsymbol{X}_r = \boldsymbol{X}_r - \boldsymbol{X}_r^{op} \tag{26}$$

$\boldsymbol{X}_m^{op}$ and $\boldsymbol{X}_r^{op}$ represent linearization points of $\boldsymbol{X}_m$ and $\boldsymbol{X}_r$. Specifically, (24) is the linear system used in the Gaussian-Newton method. By applying the Schur-Complement operation to (24), we obtain a linear system that is independent of $\boldsymbol{X}_m$.

$$\boldsymbol{H}_{rr}^*\delta\boldsymbol{X}_r = \boldsymbol{b}_r^* \tag{27}$$

$$\boldsymbol{H}_{rr}^* = \boldsymbol{H}_{rr} - \boldsymbol{H}_{rm}\boldsymbol{H}_{mm}^{-1}\boldsymbol{H}_{mr} \tag{28}$$

$$\boldsymbol{b}_r^* = \boldsymbol{b}_r - \boldsymbol{H}_{rm}\boldsymbol{H}_{mm}^{-1}\boldsymbol{b}_m \tag{29}$$

(27) can be easily converted to a prior constraint for the remaining system states, $\boldsymbol{X}_m$. From the probability perspective, $\boldsymbol{X}_m - \boldsymbol{X}_m^{op}$ follows a zero-mean Gaussian distribution.

Fig. 5 illustrates the marginalization strategy in the proposed method. In our approach, we eliminated the pose of the oldest keyframe. The relative system states contain the magnetic field vector $\boldsymbol{B}^G$, magnetometer bias $\boldsymbol{b}_B$, and pose of keyframe next to the oldest one. The relative residuals include $\boldsymbol{r}_{prior}$, $\boldsymbol{r}_{odo}$, $\boldsymbol{r}_g$, $\boldsymbol{r}_B$ and $\boldsymbol{r}_{\Delta B}$. After eliminating the oldest keyframe, the prior distribution constraint for the relative system states was added to the problem.

IV. Experiments

In this section, we present the magnetic-field vectors of the experimental scenarios. Then, we compared the proposed method to other magnetic fusion methods and verified that the proposed method can work with magnetometer measurements with biases.

The remainder of this paper is organized as follows; Section IV-A describes the test implementation in detail. Section IV-B describes the metrics used to evaluate the performance of our proposed method. Section IV-C presents the magnetic fields and compares the positioning accuracies of all methods. Section IV-D describes the effect of magnetometer biases on the proposed method. Section IV-E shows a time consumption comparison between the proposed method and the AI-IMU. Section IV-F shows the effect of the maintained keyframe numbers in graph optimization. Section IV-G summarizes the experimental results.

A. Experiment Description

An Asus Tango phone was mounted on a human head for data collection. This installation strategy aims to simulate the case of AR glasses or headsets, which are the main forms of AR devices. The Tango phone contains a global shutter fisheye camera, depth camera, IMU, and magnetometer. IMU measurements, magnetometer measurements, and ground-truth poses were collected at 100 Hz. Magnetometer measurements were calibrated using the Android API. Since the change in the phone's working state forms an additional equivalent magnetometer bias, we use the ellipsoid fitting method to manually compensate the magnetometer bias to obtain a more accurate magnetic field vector. The ground truth poses are the outputs from visual-inertial odometry. The Tango phone can use the embedded camera and IMU to estimate 3D motion through the visual-inertial odometry technique. Furthermore, it can build a visual map of the selected area and perform positioning on this map. Thus, we used the result of positioning in a pre-built map as the ground truth, if possible. Otherwise, in the scenario where the Tango phone cannot build a map, we select trajectories for which odometry can provide good positioning accuracy. We use the outputs of visual-inertial odometry as the ground truth directly.

We used the AI-IMU method described in LLIO [22] which is a lightweight version of TLIO [15]. We use the ResMLP256 LLIO-Net [22] to estimate the short-period displacement in the AI-IMU. The LLIO-Net was trained using a 40 h dataset. Six people captured the dataset using three devices in two buildings. It is worth noting that the magnetometer measurements were never used during the training of the LLIO-Net.

We compared the proposed method to several other methods. IDOL [16] is the only previous study that focused on providing accurate heading based on a magnetometer to improve learned-based inertial odometry. However, its performance degrades in new environments not contained in the training dataset, limiting the application of this technique in new environments. Furthermore, the author did not provide a pre-trained model or code at this time. Thus, we did not compare these methods. Since this paper focused on avoiding the effect of local magnetic field perturbation, we compared our method to two conventional methods to avoid the effect of local magnetic field perturbation. The details of these methods are as follows:

- AI-IMU
  The AI-IMU, as mentioned in Section III-B, is pure learning-based inertial odometry without dependency on magnetometer measurements. It is the basis for all the methods described below.
- Mag Filter
  The Mag Filter is the modification of AI-IMU, adding a measurement function using magnetometer measurements. Moreover, a χ^2-test, which is widely adopted in the Kalman Filter to avoid the effect of abnormal observations, is employed to avoid abnormal magnetometer measurements [28]. The measurement update using magnetometer measurements at t-the defined as

$$\boldsymbol{B}^N = \boldsymbol{R}_{nb_t} \boldsymbol{B}^{B_t} \tag{30}$$

  $\boldsymbol{B}^N$ is magnetic field vector in the navigation frame $\mathbf{F}^N$. It is directy given in the experiments. $\boldsymbol{B}^{B_t}$ is magnetometer measurements at moment t.
- QSF Filter
  The QSF uses magnetometer measurements based on the quasi-static field (QSF) hypothesis [20]. It detects the QSF condition, and adopts magnetic constraint in the quasi-static magnetic field. More specifically, it detects quasi-static magnetic field based on detecting changes of magnetic strength. In a quasi-static magnetic field, its measurement update at t is defined as

$$\boldsymbol{B}^{QSF} = \boldsymbol{R}_{nb_t} \boldsymbol{B}^{B_t} \tag{31}$$

  Here, $\boldsymbol{B}^{QSF}$ is magnetic field vector of current quasi-static magnetic field. It is calculated based on the first moment that detects the current quasi-static magnetic field.
- Graph-Based
  The Graph-Based is the proposed graph-optimization-based fusion algorithm. In this approach, we select one keyframe per second and keep a sliding window containing 300 keyframes.

In the remainder of this paper, we denote the ground-truth trajectory as GT.

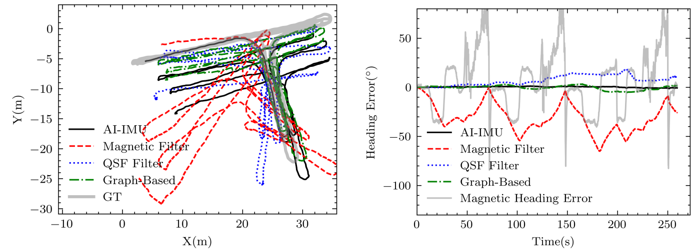

(a) (b)

Fig. 6. Illustration of Trajectory A use magnetic measurements with biases. (a) gives the trajectories of each methods. Trajectories are aligned with ground truth trajectory(GT). (b) shows the heading error of each algorithm. Magnetic Heading Error represents the heading difference between the current magnetic field vector and the reference magnetic field vector.

B. Evaluation Metric

In this study, we used the aligned average position error in the horizontal plane to evaluate the positioning performance of the aforementioned algorithms. The position of the estimated trajectory and the ground truth trajectory are represented in the navigation frame and are denoted as $\{\hat{\boldsymbol{t}}_0, \cdots, \hat{\boldsymbol{t}}_N\}$ and $\{\boldsymbol{t}_0, \cdots, \boldsymbol{t}_N\}$. $\hat{\boldsymbol{R}}_t$ and $\boldsymbol{R}$ are 2D rotation matrices. $\hat{\boldsymbol{t}}_t$ and $\boldsymbol{t}$ are 2D translations. We used the first 20% of the estimated trajectory to align with the ground truth trajectory. Specifically, we estimated the 2D rotation and translation $\{\boldsymbol{R}_a, \boldsymbol{t}_a\}$ using the following formula:

$$\{\boldsymbol{R}_a, \boldsymbol{t}_a\} = \\ \underset{\{\boldsymbol{R}_a, \boldsymbol{t}_a\}}{\arg\min} \sum_{t \in [0, 0.2N]} \{\boldsymbol{R}_a(\hat{\boldsymbol{t}}_t - \boldsymbol{t}_a) - \boldsymbol{t}_t\} \tag{32}$$

Then, the average position error is defined as:

$$\boldsymbol{e}(\hat{\boldsymbol{t}}, \boldsymbol{t}) = \frac{1}{N} \sum_{t \in [0, N]} \|\boldsymbol{R}_a(\boldsymbol{t}_t - \boldsymbol{t}_a) - \boldsymbol{t}_t\| \tag{33}$$

$\boldsymbol{R}_a$ and $\boldsymbol{t}_a$ are the aligned rotation and translation, respectively, as described in (32). $\|\cdot\|$ represents $l2$norm. The trajectory converted by $\{\boldsymbol{R}_a, \boldsymbol{t}_a\}$ is denoted as the aligned trajectory.

C. Positioning Performance

This section first compares all the methods using raw magnetometer measurements, and the results of the two trajectories shown in Fig. 6 and 7. It is noteworthy that an Android smartphone can provide calibrated magnetometer measurements, but the calibration results are variable and not always reliable. Thus, the calibrated magnetometer measurements provided by the Android systemcannot achieve the best positioning performance. Fig. 6 and 7 (a) show trajectories of all methods. Fig. 6 and 7 (b) show heading error of all methods. The magnetic heading is estimated directly by magnetometer measurements, reflecting the effect of magnetometer biases and environmental magnetic vector perturbation. The Mag Filter and QSF Filter were affected by unreliable magnetic heading, and could not provide acceptable positioning results.

To further demonstrate the robustness of the proposed methods to magnetic perturbation, we described a systematic comparison of the positioning performance of the proposed

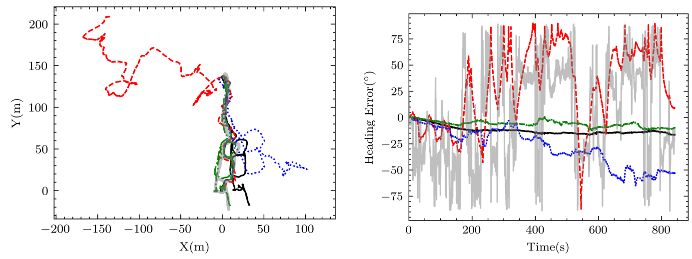

(a) (b)

Fig. 7. Illustration of Trajecotry B use magnetic measurements with biases. (a) gives the trajectories of each methods. Trajectories are aligned with ground- truth trajectory(GT). (b) shows the heading error of each algorithm. Magnetic Heading Error represents the heading difference between the current magnetic field vector and the reference magnetic field vector.

TABLE I
COMPARISON OF POSITION ERROR OF DIFFERENT ALGORITHMS.

Traj.	Length(m)	Position Error (m)			
		AI-IMU	Mag Filter	QSF Filter	Graph-Based
A	324.52	4.44	6.61	3.43	2.64
B	621.13	9.02	9.02	8.46	2.58
C	734.96	10.36	15.67	15.24	5.52
D	758.04	16.00	14.39	9.38	3.60
E	591.46	6.65	5.61	19.64	2.34
F	670.09	6.43	7.26	21.71	4.43

system with that of other methods. Other algorithms (Mag filter and QSF filter) cannot estimate acceptable results using magnetometer measurements with biases. In this comparison, the Mag Filter and QSF Filter used calibrated magnetic measurements in the following experiments, and the proposed method used magnetometer measurements with biases to demonstrate their superiority.

As mentioned in Table I, we used six trajectories at different locations and with different shapes to evaluate the magnetic fusion results. Trajectory A involves walking in a small office building where the Tango phone can construct a pre-built map. All trajectories were walked for a long time to ensure that the heading drift caused a significant positioning error. The proposed method (graph-based) showed the smallest positioning error in all cases. The position error of the graph-based method (the proposed method) was significantly smaller than those of the other methods. Fig. 8 shows the cumulative distribution function(CDF) of position error of all trajectories. The performance of the graph-based method was better than that of the other methods. Furthermore, the performance of the Mag Filter and QSF Filter was not stable. The QSF filter showed better accuracy than the Mag filter in trajectories A, B, C, and D. In contrast, for trajectories E and D, the Mag filter showed better accuracy.

Fig. 9 and Fig. 10 give detail of the magnetic field vector and comparison between algorithms. Fig. 9 (a) and Fig. 10 (a) show the local magnetic field vector. It is calculated based on the magnetometer measurements $\boldsymbol{B}^{B_t}$ and rotation matrix $\boldsymbol{R}_{nb_t}$ of the ground truth trajectory. The local magnetic field vector $\boldsymbol{B}_{local}^N$ is defined as follows:

$$\boldsymbol{B}_{local}^N = \boldsymbol{R}_{nb_t} \boldsymbol{B}^{B_t} \tag{34}$$

The magnetic field vector is roughly consistent, but perturbated at some positions. Thus, it is proven that the average magnetic field vector in the sub-areas is only limitedly affected by the magnetic field perturbation.

Fig. 9 (b) and Fig. 10 (b) show angle difference between each method and ground truth. We calculated the angle difference based on the aligned trajectory for each method, as mentioned in Section IV-B. To illustrate the effect of the local magnetic field vector heading, we provide the heading difference between the local magnetic field vector and reference magnetic field vector. This heading difference is denoted as the magnetic heading error in Fig. 9 (b) and Fig. 10 (b). In Table II, we provide the average heading error and corresponding magnetic field vector heading difference, which represents the difference between the reference heading and the heading estimated based on magnetometer observations.

Because the Mag filter directly uses magnetometer measurements in the measurement update, its heading is easily affected by magnetic field perturbation. Meanwhile, its heading was slightly better than the heading direction of the magnetic field vector heading. The Kalman filter simultaneously estimates the current heading based on the compressed prior information and the current magnetic field vector heading. In other words, the heading is the weighted average of the previous magnetic headings. As shown in Fig. 9 (c) and Fig. 10 (c), its position accuracy is significantly degraded because of the heading perturbation.

QSF filters are robust to magnetic-field perturbations because they do not use magnetic constraints when the magnetic field varies. The heading error of the QSF filter increases over time because the QSF does not use a globally consistent reference magnetic field vector. Although QSF is not easily affected by local magnetic field perturbation, its heading error is higher than that of the Mag filter in the long term.

The proposed method(graph-based) is robust to magnetic field perturbations and does not drift over time. This shows the best relative accuracy of heading estimation. However, it may maintain a heading bias related to the ground truth heading. This bias was caused by the difference between the global average magnetic field vector and the average magnetic field vector at the beginning of the experiment. In other words, the average magnetic field vector during the first sliding window contains bias in other areas. We evaluated the position accuracy and used an aligned trajectory to avoid this problem. In Fig. 9 (c) and Fig. 10 (c), the aligned trajectories show that Graph-Based provides the best relative positioning accuracy in the experiments.

In the experiments, the graph-based method, which uses uncalibrated magnetometer measurements, shows better performance than other methods that use calibrated magnetometer measurements.

D. Effect of magnetometer biases

Because the proposed method models the biases in the proposed method, it can localize the user even when the magnetometer measurements contain biases. As mentioned before, the graph-based method uses magnetometer measurements

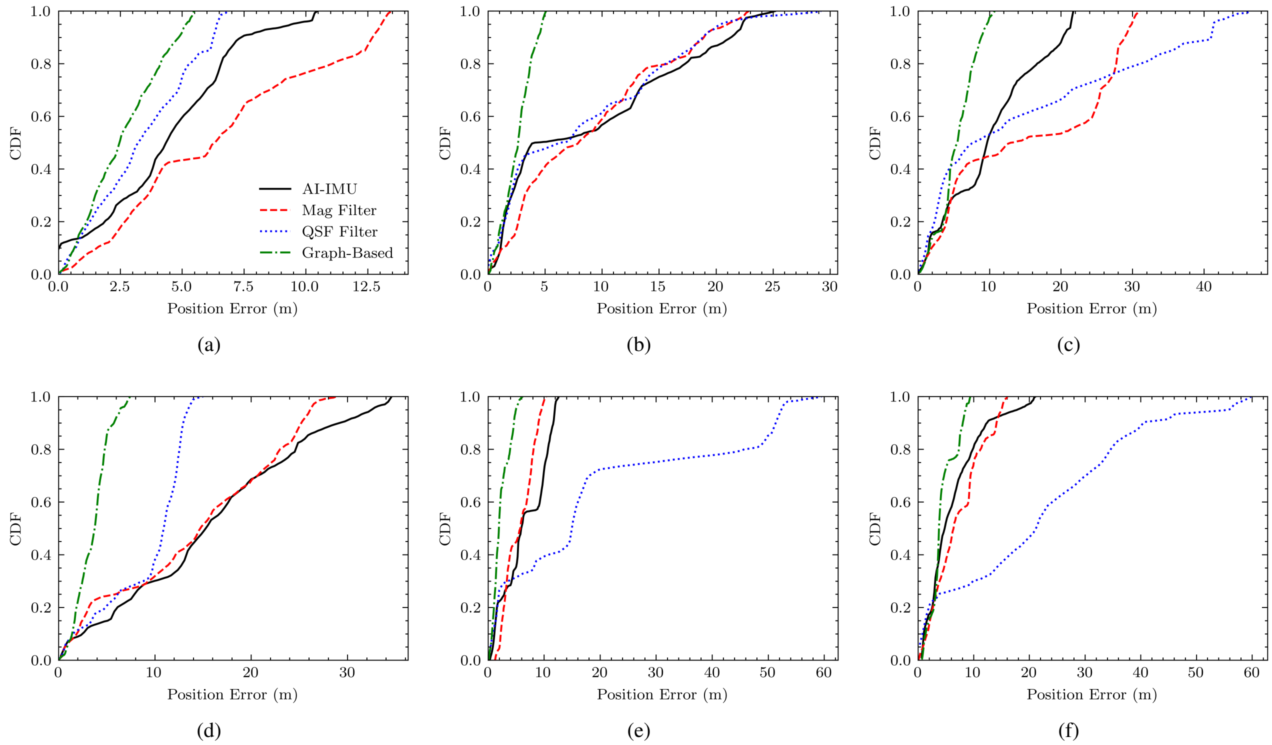

Fig. 8. Illustration of CDF of all trajectories. (a), (b), (c), (d), (e), and (f) represent CDF of trajectory A, B, C, D, E, and F, respectively.

TABLE II
COMPARISON OF HEADING ERROR OF DIFFERENT ALGORITHMS.

Traj.	Length(m)	Heading Error (°)				Magnetic Field Vector Heading Difference (°)
		AI-IMU	Mag Filter	QSF Filter	Graph-Based	
A	324.52	0.40	3.06	3.12	2.05	6.18
B	621.13	6.42	4.58	9.62	2.66	7.61
C	734.96	3.58	3.51	18.55	3.49	13.16
D	758.04	12.76	8.39	4.12	2.71	3.37
E	591.46	1.50	3.02	24.99	1.92	4.89
F	670.09	8.00	2.63	16.99	2.32	10.09

with a known bias in the test. The bias is $[30, -20, 30]\mu T$. Table I lists the estimated magnetometer bias of the graph based on each trajectory. Fig. 9 (d) and Fig. 10 (d) give the variation of estimated magnetometer bias over time in trajectory A and B. We precisely estimated the y-and z-components of the magnetometer biases. However, the x-component converges slowly or does not converge to a given value. This phenomenon may be because the x-axis is roughly oriented upward. During the walking process, changes in the pitch and roll angles were limited. Thus, the observability of the x axis is weak. In some cases, the x-component of the magnetometer bias may be unobservable without the constraint of the magnetic field vector norm $\|\boldsymbol{B}^G\|$. Fortunately, the x-component does not significantly influence the heading estimation when its observability is weak.

Table III lists the estimated magnetometer bias and position error of Graph-based trajectories A, B, and C. The first column shows the magnetic biases in the magnetometer measurements for the graph-based optimization. Graph-based devices show similar performance at different given magnetic biases. This indicates that the proposed method is robust to the magnetometer bias.

E. Computational Cost

Because the proposed method aims to run on mobile devices, the computational cost should be considered. Table IV shows the time consumption of each block of the proposed method (graph-based) during the run trajectory F. The method was executed on a desktop computer equipped with an octa-core CPU(i7-10700k). The total time length of trajectory F is 866 s. The proposed method costs 32.38 seconds. It runs 27× in real time on a computer. The proposed method combines an AI-IMU with an additional graph-optimization-based estimator to fuse magnetometer measurements. The AI-IMU consists of propagation (Section III-B2), measurement udpate(Section III-B3), and network inference (8) blocks. The bottleneck of the AI-IMU is the network inference module, which requires 18 seconds. The grah-optimization-based estimator is denoted as graph-optimization in Table IV. This block, described in Section III-C, contains graph generation, graph optimization, and marginalization blocks. It costs 11.5 ms per time, but only runs at 1 Hz. Thus, its total cost time is 30 s, which

TABLE III
PERFORMANCE OF EACH TRAJECTORIES WITH DIFFERENT MAGNETIC BIASES

Given Magnetometer Bias		A	B	C
[30,-10,30]	Position Error (m)	2.64	2.59	5.53
	Magnetometer Bias (μT)	[24.8,-9.3,29.1]	[29.2,-10.2,30.3]	[31.3,-10.2,29.7]
[30,-20,30]	Position Error (m)	2.64	2.58	5.52
	Magnetometer Bias (μT)	[24.8,-19.4,29.2]	[29.2,-20.3,30.4]	[31.3,-20.2,29.8]
[30,-30,30]	Position Error (m)	2.64	2.59	5.52
	Magnetometer Bias (μT)	[24.8,-29.3,29.1]	[29.1,-30.2,30.3]	[31.3,-30.2,29.8]
[30,-40,30]	Position Error (m)	2.65	2.56	5.53
	Magnetometer Bias (μT)	[24.8,-39.3,29.1]	[29.2,-40.2,30.3]	[31.3,-40.1,29.7]
[30,-50,30]	Position Error (m)	2.66	2.56	5.53
	Magnetometer Bias (μT)	[24.8,-49.3,29.2]	[29.2,-50.2,30.3]	[31.3,-50.2,29.8]
[30,-60,30]	Position Error (m)	2.64	2.56	5.52
	Magnetometer Bias (μT)	[24.8,-59.3,29.1]	[29.2,-60.2,30.3]	[31.3,-60.2,29.8]

TABLE IV
TIME CONSUMPTION OF THE PROPOSED METHOD.

	AI-IMU			Graph-Optimization	Total
	Propagation	Measurement Update	Network Inference		
Average Time (millisecond)	0.013	0.34	2.10	11.5	-
Count	86664	8647	8657	867	-
Totally Time (second)	1.17	2.99	18.21	10.01	32.38
Ratio (%)	3.61	9.23	56.24	30.38	-

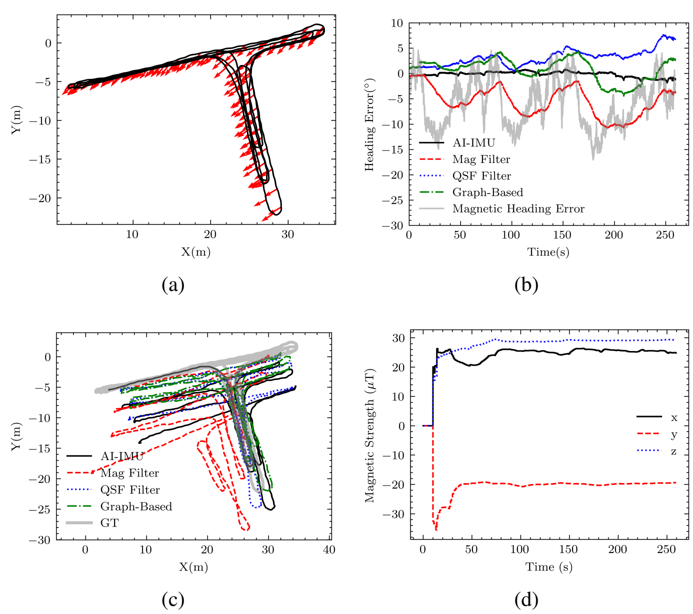

Fig. 9. Illustration of Trajectory A. (a) shows reference trajectory and local magnetic field vector at some point. (b) shows the heading error of each algorithm. Magnetic Heading Error represents the heading difference between the current magnetic field vector and the reference magnetic field vector. (c) gives the trajectories of each method. Trajectories are aligned with ground truth trajectory (GT). (d) shows the estimated magnetometer bias $\boldsymbol{b}_B$ outputted by the proposed method (Graph-Based). The true value of magnetometer bias is $[30, -20, 30]$.

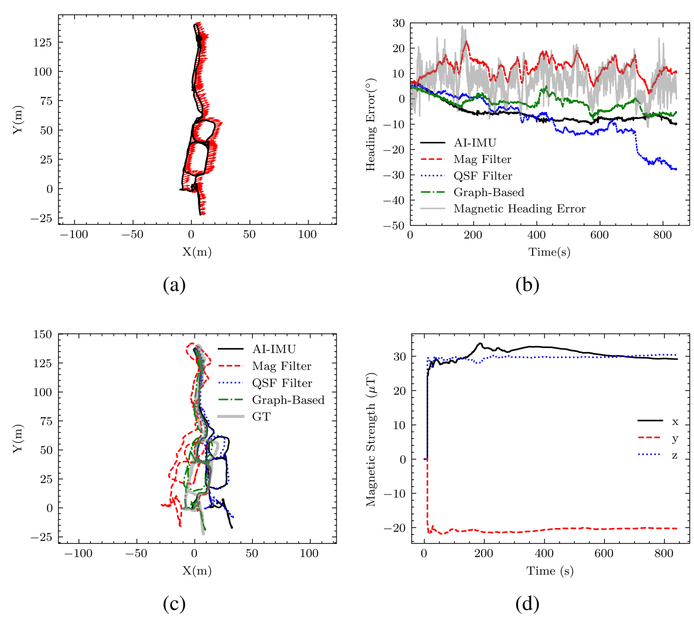

Fig. 10. Illustration of Trajectory B. (a) shows reference trajectory and local magnetic field vector at some point. (b) shows the heading error of each algorithm. Magnetic Heading Error represents the heading difference between the current magnetic field vector and the reference magnetic field vector. (c) gives the trajectories of each method. Trajectories are aligned with ground truth trajectory (GT). (d) shows the estimated magnetometer bias $\boldsymbol{b}_B$ outputted by the proposed method (Graph-Based). The true value of magnetometer bias is $[30, -20, 30]$.

is less than that of the AI-IMU blocks. In summary, the time consumption of the added graph-based optimization block did not significantly exceed that of the AI-IMU. Meanwhile, the resource-demanding computation of the proposed method is acceptable for running on mobile devices.

F. Effect of sliding window size

The proposed method uses a sliding window to maintain magnetometer measurements over the long term and achieves a reliable heading estimation. The sliding window size is related to the stability of heading estimation and position accuracy. Fig. 11 gives the relation between position error and size of sliding windows. When the number of keyframes is less

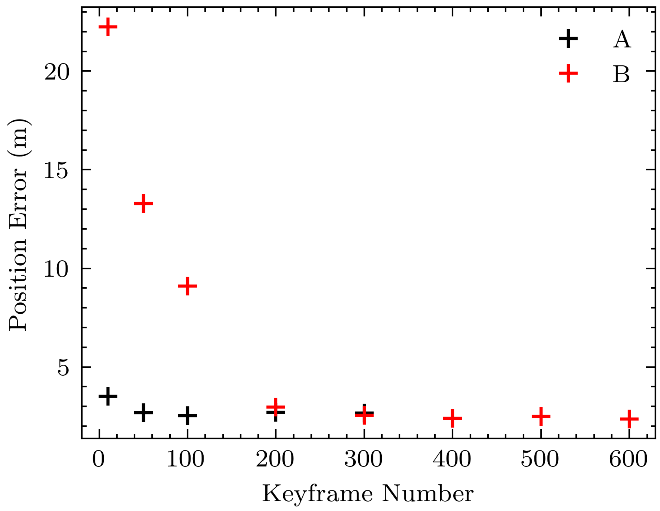

Fig. 11. Relation between position error and maintained keyframe number of trajectory A and B.

than 200, an increase in keyframes can significantly reduce the position error. When the number of keyframes is greater than 200, the increase in the number of keyframes has only a limited impact on the positioning accuracy. The results for Trajectory A do not include experiments with more than 300 keyframes because the entire dataset length does not reach 300 s. In other experiments, we used 300 keyframes.

G. Discussion

The robustness of magnetic field perturbation is the main advantage of the proposed method. As shown in Fig. 9 (a) and Fig. 10 (a), the phenomenon that the average magnetic field in a large area can reflect the heading is determined in these two experiment environments. Indeed, this phenomenon was satisfied in all six experimental trajectories collected in four different buildings. Under this condition, the proposed method can constrain heading in areas with local magnetic field perturbation and provide better position accuracy than the others, as mentioned in Section IV-C.

Another advantage of this method is that the magnetometer bias can be estimated online, as listed in Table III. Thus, this method can be used on magnetometers, whether calibrated or not, such as those installed in smartphones or AR headsets. This situation is common for consumer-grade devices.

The proposed method combines the AI-IMU and graph-optimization modules. This design helps the proposed method achieve a trade-off between the accuracy and computational cost. The characteristics of the magnetic field are that the local magnetic field is highly perturbated, and the long-term magnetic field is stable. To utilize this characteristic to achieve a stable and no-drift heading estimation, we should maintain magnetometer measurements in the long term, as shown in Section IV-F. The AI-IMU relies on high-frequency measurement updates, such as 10 Hz, using the network outputs to ensure accuracy and reliability. However, it is impossible to achieve these two targets using a single estimator. Therefore, a two-stage fusion strategy was designed. The AI-IMU module outputs high-frequency pose estimation, and the graph-optimization module runs at a low frequency to fuse the output relative poses of the AI-IMU and magnetometer measurements. Thus, the proposed method achieved a significant positioning accuracy improvement for the AI-IMU but only slightly increased the computational cost, as mentioned in Table IV.

V. Conclusion

A graph-optimization-based estimator was proposed to fuse the AI-IMU and magnetometer. The proposed method can use the heading based on magnetometer observations to improve the pose estimation performance of AI-IMU in indoor environments. The reasons include: 1) The proposed method makes use of the fact that the magnetic interference is zero-mean and uses a sliding window to suppress the effect of the magnetic field perturbation. 2) The proposed method estimates the magnetometer biases online to deal with the magnetometer bias change caused by the working state switches of the smartphone. The test results show that the proposed method, even when using uncalibrated magnetometer observations, still achieves the best position accuracy in all tested scenarios compared to the existing methods that use calibrated observations. Moreover, to satisfy the requirements of real-time positioning, we analyzed the time consumption of each module of the proposed method. The test results show that the proposed method can run 27$\times$ faster than real time on a desktop computer and does not significantly exceed the time consumption of the AI-IMU. Therefore, its computational load is acceptable for real-time operations.

In future work, because the sliding window length of the proposed method is limited, the phenomenon in which the average magnetic field vector is not affected by magnetic field perturbation may not be valid in some cases. For example, when a pedestrian walks around a small area with similar magnetic-field biases, these biases cannot be mitigated within the sliding window. Fortunately, these exceptional cases may not appear frequently in the literature. Moreover, we will focus on the tightly coupled fusion of the neural network, IMU mechanism, and magnetometer measurements to obtain a more stable and high-performance pose estimation.

References

[1] T. Shan and B. Englot, “Lego-loam: Lightweight and ground-optimized lidar odometry and mapping on variable terrain,” in *2018 IEEE/RSJ International Conference on Intelligent Robots and Systems (IROS)*. IEEE, 2018, pp. 4758–4765.

[2] T. Shan, B. Englot, D. Meyers, W. Wang, C. Ratti, and D. Rus, “Lio-sam: Tightly-coupled lidar inertial odometry via smoothing and mapping,” in *2020 IEEE/RSJ International Conference on Intelligent Robots and Systems (IROS)*. IEEE, 2020, pp. 5135–5142.

[3] R. Mur-Artal and J. D. Tardós, “Orb-slam2: An open-source slam system for monocular, stereo, and rgb-d cameras,” *IEEE Trans. Robot.*, vol. 33, no. 5, pp. 1255–1262, 2017.

[4] T. Qin, P. Li, and S. Shen, “Vins-mono: A robust and versatile monocular visual-inertial state estimator,” *IEEE Trans. Robot.*, vol. 34, no. 4, pp. 1004–1020, 2018.

[5] A. I. Mourikis and S. I. Roumeliotis, “A multi-state constraint kalman filter for vision-aided inertial navigation,” in *Proceedings 2007 IEEE International Conference on Robotics and Automation*. IEEE, 2007, pp. 3565–3572.

[6] D. Zuñiga-Noël, A. Jaenal, R. Gomez-Ojeda, and J. Gonzalez-Jimenez, "The uma-vi dataset: Visual–inertial odometry in low-textured and dynamic illumination environments," *The International Journal of Robotics Research*, vol. 39, no. 9, pp. 1052–1060, 2020.
[7] Y. Wang and X. Li, "An improved robust ekf algorithm based on sigma points for uwb and foot-mounted imu fusion positioning," *Journal of Spatial Science*, vol. 66, no. 2, pp. 329–350, 2021.
[8] J. Liu, K. Gao, W. Guo, J. Cui, and C. Guo, "Role, path, and vision of "5g+ bds/gnss"," *Satellite Navigation*, vol. 1, no. 1, pp. 1–8, 2020.
[9] P. D. Groves, "Principles of gnss, inertial, and multisensor integrated navigation systems, [book review]," *IEEE Aerospace and Electronic Systems Magazine*, vol. 30, no. 2, pp. 26–27, 2015.
[10] J. Kuang, X. Niu, and X. Chen, "Robust pedestrian dead reckoning based on mems-imu for smartphones," *Sensors*, vol. 18, no. 5, p. 1391, 2018.
[11] A. Martinelli, H. Gao, P. D. Groves, and S. Morosi, "Probabilistic context-aware step length estimation for pedestrian dead reckoning," *IEEE Sensors journal*, vol. 18, no. 4, pp. 1600–1611, 2017.
[12] X. Hou and J. Bergmann, "Pedestrian dead reckoning with wearable sensors: A systematic review," *IEEE Sensors Journal*, vol. 21, no. 1, pp. 143–152, 2020.
[13] C. Chen, X. Lu, A. Markham, and N. Trigoni, "Ionet: Learning to cure the curse of drift in inertial odometry," in *Proceedings of the AAAI Conference on Artificial Intelligence*, vol. 32, no. 1, 2018.
[14] S. Herath, H. Yan, and Y. Furukawa, "Ronin: Robust neural inertial navigation in the wild: Benchmark, evaluations, & new methods," in *2020 IEEE International Conference on Robotics and Automation (ICRA)*. IEEE, 2020, pp. 3146–3152.
[15] W. Liu, D. Caruso, E. Ilg, J. Dong, A. I. Mourikis, K. Daniilidis, V. Kumar, and J. Engel, "Tlio: Tight learned inertial odometry," *IEEE Robot. Autom. Lett.*, vol. 5, no. 4, 2020.
[16] S. Sun, D. Melamed, and K. Kitani, "Idol: Inertial deep orientation-estimation and localization," in *Proceedings of the AAAI Conference on Artificial Intelligence*, vol. 35, no. 7, 2021, pp. 6128–6137.
[17] Y. Wang, H. Cheng, C. Wang, and M. Q.-H. Meng, "Pose-invariant inertial odometry for pedestrian localization," *IEEE Transactions on Instrumentation and Measurement*, vol. 70, pp. 1–12, 2021.
[18] M. Ma, Q. Song, Y.-h. Li, and Z.-m. Zhou, "Magnetic field aided heading estimation for indoor pedestrian positioning," in *2017 IEEE 2nd Information Technology, Networking, Electronic and Automation Control Conference (ITNEC)*, 2017, pp. 919–923.
[19] B. Candan and H. E. Soken, "Robust attitude estimation using imu-only measurements," *IEEE Transactions on Instrumentation and Measurement*, vol. 70, pp. 1–9, 2021.
[20] M. H. Afzal, V. Renaudin, and G. Lachapelle, "Use of earth's magnetic field for mitigating gyroscope errors regardless of magnetic perturbation," *Sensors*, vol. 11, no. 12, pp. 11 390–11 414, 2011.
[21] J. B. Bancroft and G. Lachapelle, "Use of magnetic quasi static field (qsf) updates for pedestrian navigation," in *Proceedings of IEEE/ION PLANS 2012*, 2012, pp. 605–612.
[22] Y. Wang, J. Kuang, and xiaoji niu, "LLIO: Lightweight Learned Inertial Odometer," 8 2021. [Online]. Available: https://www.techrxiv.org/articles/preprint/LLIO_Lightweight_Learned_Inertial_Odometer/16408383
[23] P. J. Huber, "Robust estimation of a location parameter," in *Breakthroughs in statistics*. Springer, 1992, pp. 492–518.
[24] K. Levenberg, "A method for the solution of certain non-linear problems in least squares," *Quarterly of applied mathematics*, vol. 2, no. 2, pp. 164–168, 1944.
[25] D. W. Marquardt, "An algorithm for least-squares estimation of nonlinear parameters," *Journal of the society for Industrial and Applied Mathematics*, vol. 11, no. 2, pp. 431–441, 1963.
[26] S. Agarwal, K. Mierle, and Others, "Ceres solver," http://ceres-solver.org.
[27] S. Leutenegger, S. Lynen, M. Bosse, R. Siegwart, and P. Furgale, "Keyframe-based visual–inertial odometry using nonlinear optimization," *The International Journal of Robotics Research*, vol. 34, no. 3, pp. 314–334, 2015.
[28] B. Brumback and M. Srinath, "A chi-square test for fault-detection in kalman filters," *IEEE Transactions on Automatic Control*, vol. 32, no. 6, pp. 552–554, 1987.

Yan Wang received the B.Eng. degree in Chemical Engineering and Technology from China University of Mining and Technology, Xuzhou, China, in 2016. And he received an M.S. degree in Computer Applied Technology from China University of Mining and Technology, Xuzhou, China, in 2019. He is currently pursuing a Ph.D. degree in GNSS Research Center, Wuhan University, Wuhan, China. His research interests focus on indoor Navigation, sensor fusion algorithm, and computer vision.

Jian Kuang received the B.Eng. degree and Ph.D. degree in Geodesy and Survey Engineering from Wuhan University, Wuhan, China, in 2013 and 2019, respectively. He is currently a Postdoctoral Fellow with the GNSS Research Center in Wuhan University, Wuhan, China. His research interests focus on inertial Navigation, pedestrian navigation, and indoor positioning.

You Li (Member, IEEE) received the B.Eng. degreefrom the China University of Geoscience (Beijing)in 2009, and the Ph.D. degree from Wuhan Uni-versity and the University of Calgary in 2015 and2016, respectively. He is currently a Professor withthe State Key Laboratory of Information Engineer-ing in Surveying, Mapping and Remote Sensing(LIESMARS), Wuhan University, China. He hashosted/participated in five national research projects,and co-published over 70 academic articles and hasover 20 patents pending. His research focuses onpositioning and motion-tracking techniques and their uses in the IoT devices,smartphones, robots, and cars. He serves as a committee member for the IAGunmanned navigation systems and ISPRS mobile mapping working groups,and an Associate Editor for the IEEE SENSORSJOURNAL.

Xiaoji Niu received the B.Eng. degree (with honors) in Mechanical and Electrical Engineering and the Ph.D. from Tsinghua University, Beijing, China. He was a Postdoctoral Fellow with the Mobile MultiSensor Systems (MFMSS) Research Group, Department of Geomatics Engineering, and the University of Calgary. He was a Senior Scientist with SiRF Technology, Inc. At present, he is a professor of the GNSS Research Center and the Artificial Intelligent Institute at Wuhan University, Wuhan, China. His research interests focus on INS, GNSS/INS integration for land vehicle navigation, and pedestrian navigation.